Frequency Dependence of the Structure and Temporal Development of Wintertime Tropospheric Fluctuations—Comparison of a GCM Simulation with Observations

NGAR-CHEUNG LAU AND MARY JO NATH

Geophysical Fluid Dynamics Laboratory/NOAA, Princeton University, Princeton, NJ 08542

(Manuscript received 20 May 1986, in final form 24 July 1986)

ABSTRACT

The three-dimensional structure and temporal evolution of tropospheric fluctuations appearing on various time scales in observed and model-simulated atmospheres are investigated using cross-spectral analyses. The datasets examined include NMC analyses of the 500 mb height and sea level pressure fields for 18 winters, as well as a 12-winter simulation of the same fields by a 15-wavenumber general circulation model at GFDL. Statistically significant phase differences between 500 mb height fluctuations at selected centers of action and the corresponding fluctuations at all other grid points are displayed for various frequency bands using a vectorial format. Similar plots are constructed to elucidate the vertical phase structure in the middle and lower troposphere at individual grid points, as well as the propagation characteristics of the sea level pressure field in the vicinity of sloping terrain. It is demonstrated that these phase/coherence diagrams offer a useful alternative for quantifying the lead/lag relationships between different anomaly centers associated with some of the well-known teleconnection patterns.

The spectral results presented here indicate that the spatial and temporal behavior of the Pacific/North American, Atlantic and Northern Asian Patterns, as documented in various recent studies, exhibit a notable frequency dependence in both real and model atmospheres. For periods of 27–80 days, the atmospheric variability over the Pacific and Atlantic Basins is organized in north–south oriented dipoles, with an almost 180° out-of-phase relationship between oscillations at the opposite poles. As attention is shifted to the 20- and 10-day time scales, the north–south seesaw pattern gradually weakens, and all three teleconnection patterns mentioned above are characterized by successive downstream development from west to east of alternating troughs and ridges. Fluctuations with periods longer than 20 days acquire an equivalent barotropic structure over much of the northern oceans, with in-phase variations at 500 mb and at sea level.

The eddy behavior undergoes still further changes as one considers the 4-day period band. The high frequency disturbances tend to be elongated in the meridional direction. The corresponding horizontal phase variations are indicative of continuous eastward propagation across the midlatitude oceans and northern Siberia. The vertical phase variations suggest a systematic transition from a distinctly baroclinic structure at the starting points of such cyclone tracks, to a more barotropic structure in regions farther east.

The perturbations near the eastern and northern peripheries of the Tibetan Plateau are noted for their weak coherence in the vertical direction. Horizontal phase diagrams based on sea level pressure data reveal that the path of near-surface fluctuations tends to be aligned parallel to the local topographic contours in this region.

Comparison between model and observational results indicates that the GCM examined here is capable of reproducing the frequency and geographical dependence of the principal modes of variability in the Northern Hemisphere wintertime circulation.

1. Introduction

The strong dependence of the nature of atmospheric variability on geographical location and on time scale has long been recognized. Klein (1951) has documented the standard deviations and lagged autocorrelations of pressure fluctuations on daily time scales, and noted that the spatial patterns of such statistics in the Western Hemisphere are dominated by the synoptic disturbances migrating along the cyclone track extending from the Great Lakes to Iceland. By examining the behavior of perturbations with periods between 15 and 60 days, Sawyer (1970) showed that the centers of maximum amplitude, three-dimensional structure, as well as temporal evolution of these low-frequency circulation features also exhibit a strong geographical dependence. Furthermore, comparison between the findings reported in the two studies cited above reveals substantial differences between fluctuations in various frequency regimes. Whereas the interdiurnal changes in Klein's investigation are largely attributable to the passage of transitory weather systems, the results presented by Sawyer apparently portray another family of atmospheric phenomena, of which blocking flows and teleconnections between remote "centers of action" are notable examples.

With the availability of more comprehensive datasets and computer-aided data processing techniques, the last decade has seen a rapid expansion of our empirical knowledge of the properties of circulation features with various time scales. In particular, many diagnostic studies have been performed using gridded synoptic

analyses produced on a routine basis by various operational weather centers, such as the U.S. National Meteorological Center, the European Centre for Medium-Range Weather Forecasts, and the Australian Weather Bureau. Investigations based on these data archives include

- Documentation of the three-dimensional distributions of temporal mean, variance and covariance statistics of the atmospheric circulation, and evaluation of the relative contributions of fluctuations in different frequency bands to these local transient eddy statistics (e.g., Blackmon, 1976; Blackmon et al., 1977; Lau, 1978 and 1979; Trenberth, 1981 and White, 1982). These studies have provided detailed information on midlatitude cyclone tracks, as well as preferred regions of cyclogenesis and blocking in both hemispheres and for both the winter and summer seasons. Much light has also been shed on the geographical relationships between these transient phenomena and the stationary flow.
- Diagnosis of the spatial structure and temporal evolution of time-filtered atmospheric perturbations, as revealed by empirical orthogonal functions, teleconnection patterns, composites, lagged correlation statistics and other pattern recognition techniques (e.g., O'Conner, 1969; van Loon and Rogers, 1978; Wallace and Gutzler, 1981; Namias, 1981; Esbensen, 1984; and Blackmon et al., 1979, 1984a,b). These studies have identified the shape, three-dimensional configuration and propagation characteristics of various modes of variability.

Physical interpretation of the multitude of phenomena uncovered by the observational studies mentioned above has been facilitated by concurrent advances in our theoretical understanding of different types of atmospheric motions. For instance, the structure, propagation characteristics and transport properties of model-generated baroclinic waves (Simmons and Hoskins, 1978; Frederiksen, 1979) are consistent with the behavior of observed midlatitude perturbations with periods shorter than about a week. On the other hand, the signatures of atmospheric fluctuations with time scales ranging from 10 days to a season are apparently associated with a variety of dynamical mechanisms which are rather distinct from baroclinic instability. The processes relevant to low-frequency atmospheric variability include Rossby wave dispersion (Hoskins et al., 1977), barotropic instability of quasi-stationary waves (Simmons et al., 1983), three-dimensional instability (Fredericksen, 1982, 1983), and remote or local forcing accompanying anomalous boundary conditions at the air–sea and air–land interfaces (Hoskins and Karoly, 1981).

The advent of high-speed computers and efficient model design have enabled various General Circulation Model (GCM) research groups to perform experiments with durations comparable to the length of existing observational weather records. These multiyear numerical integrations reflect our state-of-the-art capability in simulating various components of the climate system. In assessing the fidelity of these model runs, a natural question to ask is whether the observed frequency dependence of the spatial and temporal characteristics is realistically simulated in the model atmosphere, and whether the dynamical processes examined in simplified mechanistic models are still discernible in complex GCMs. Blackmon and Lau (1980) analyzed the history tapes for a 120-day integration with a grid point GCM developed at the Geophysical Fluid Dynamics Laboratory (GFDL) and documented the contributions to the total model variance by disturbances with various temporal and spatial scales. In that study, a definitive evaluation of the model performance at the low-frequency end of the spectrum was somewhat handicapped by the inadequate sampling of the long-period phenomena within a single winter. This restriction was removed as more extended integrations with spectral models were completed. Equipped with a 15-year GCM integration at GFDL, Manabe and Hahn (1981) were able to document the amplitudes of simulated atmospheric variability of daily, monthly and annually averaged quantities. Parallel efforts were also launched at the National Center for Atmospheric Research (NCAR) by Malone et al., (1984) to examine the transient behavior in the model atmosphere with the full range of time scales from several days to a season.

Comparisons of atmospheric variability in model and observed atmospheres have thus far been largely confined to the construction of spectra (Pratt, 1979; Hayashi and Golder, 1977) and to the mapping of variance and covariance patterns (Manabe and Hahn, 1981; Malone et al., 1984). In light of the observational results reported in recent literature, an even more stringent test of model performance should entail diagnoses of the shape and space/time evolution of the individual simulated atmospheric entities, and of the dependence of such eddy properties on geographical location and on characteristic time scale. The present study is an attempt in this direction. By applying an identical set of analysis tools to long series of observed and simulated data records, we shall evaluate the extent to which a spectral GCM is able to mimic various aspects of eddy behavior detected in nature during the Northern Hemisphere winter. In the course of this investigation, ample use has been made of the cross-spectral technique to ascertain the spectral dependence of coherence and phase relationships between fluctuations at different sites. We shall presently demonstrate that this technique is a useful alternative for identifying many of the eddy characteristics discerned in various observational studies based on other methods. Hence, the results presented here not only serve to verify the model simulation against observations, but also to complement other observational studies in the published literature by illustrating the considerable degree of consistency among findings drawn from different diagnostic techniques.

The observational and model datasets as well as the analysis procedures used in this study are described in section 2. Mean and variance statistics for the Northern Hemisphere wintertime circulation are presented in section 3. The centers of action for the observed and simulated geopotential height fluctuations in the middle troposphere are identified in section 4. Horizontal coherence/phase patterns associated with selected centers of action and with different frequency bands are discussed in section 5. Regional characteristics of the vertical phase structure and their frequency dependence are explored in section 6. Orographic influences on the propagation of near-surface disturbances are investigated in section 7, followed by a concluding section in which the principal results are discussed in relation to findings reported in other studies.

2. Datasets and analysis procedures

The observational database consists of twice-daily gridded analyses of 500 mb geopotential height and sea level pressure produced by the National Meteorological Center (NMC) for 18 winters from 1963/64 to 1980/81. The data grid used has a resolution of 5° and 2.5° in the zonal and meridional directions, respectively, and extends from 20° to 90°N. The winter season is defined as the 120-day period starting from November 15. Missing data grids in the time series have been filled by linear interpolation in time.

The model results presented in this study are based on daily grids of 515 mb geopotential height and sea level pressure for the first 12 winters of a 15-year integration with a GCM developed at GFDL. The definition of the winter season is the same as that adopted for the NMC analyses. The GCM used for generating this dataset is a 9-level spectral model with a rhomboidal truncation at 15 wavenumbers. The resolution for the corresponding Gaussian grid is approximately 7.5° in longitude and 4.5° in latitude. The model domain is global, but only results for the region north of 20.25°N are presented. A detailed description of the model formulation has been given by Gordon and Stern (1982). The essential features and physical processes incorporated in this model include: realistic distributions of continents and oceans, orography, a comprehensive hydrological cycle, moist and dry convection, sea ice formation, radiative transfer, as well as exchange of momentum, moisture, and latent and sensible heat at the lower boundary. The amount of cloud cover is prescribed to be a function of height and latitude only. Throughout the course of the integration examined here, the model environment has been subjected to a set of external forcings evolving through repetitive, identical annual cycles. Hence, the prescribed seasonal values of the solar input at the top of the atmosphere and the sea surface temperature in the World Oceans do not vary from year to year.

In order to investigate transient features with temporal scales residing in specific frequency bands, two sets of digital time filters were applied to the time series described above. The first set, hereafter referred to as the "bandpass" filter, is used to retain synoptic scale fluctuations with periods ranging from 2.5 to 6 days. The second set, to be referred to as the "lowpass" filter, has a maximum response for periods of 10 days and longer. For a convenient comparison with earlier results, the twice-daily NMC analyses were subjected to the same 31-point filters used by Blackmon (1976, Table 1, first and second columns) and several subsequent studies. Similarly, the filters for the once-daily GCM grids consist of 21 points, with coefficients being identical to those given by Blackmon and Lau (1980, Table 1). For both observational and model data, the climatological seasonal variations were estimated by subdividing each 120-day winter season into 24 consecutive, nonoverlapping 5-day means, and then computing the multiyear averages for each of these 24 pentads. The climatological seasonal cycle thus obtained was subsequently removed from the lowpass filtered data by calculating deviations of the daily or twice-daily values from the long-term means of the appropriate pentads in the winter calendar. The lowpass datasets examined in this study hence describe fluctuations with periods from 10 days to a season, as well as variability among different winter seasons.

TABLE 1. Locations of reference points for constructing phase/coherence patterns in the observed and model atmospheres.

Pattern	Observation	Model
Pacific/North American (PNA)	50°N 170°W	47.25°N 157.5°W
Atlantic (AL)	55°N 30°W	47.25°N 30.0°W
Northern Asian (NA)	60°N 60°E	60.75°N 60.0°E

3. Mean and variance statistics

The present study is not intended to be an exhaustive documentation of the observed and model climatology. We shall confine our attention to a selected set of circulation statistics which are directly relevant to the results shown in the later sections. The interested reader is referred to Manabe and Hahn (1981) and Lau (1981) for a more thorough description of the stationary and transient components of the simulated circulation in this experiment. In Fig. 1 are shown the observed distributions of the departure from zonal symmetry of the time-averaged 500 mb height (panel a), as well as the rms 500 mb height as computed using lowpass (panel c) and bandpass (panel e) filtered data. The corresponding results based on GCM data are presented in panels (b), (d) and (f). The maxima and minima in Figs. 1a and 1b depict the locations of the stationary ridges and troughs, respectively. Comparison between these two patterns reveals that most of the observed

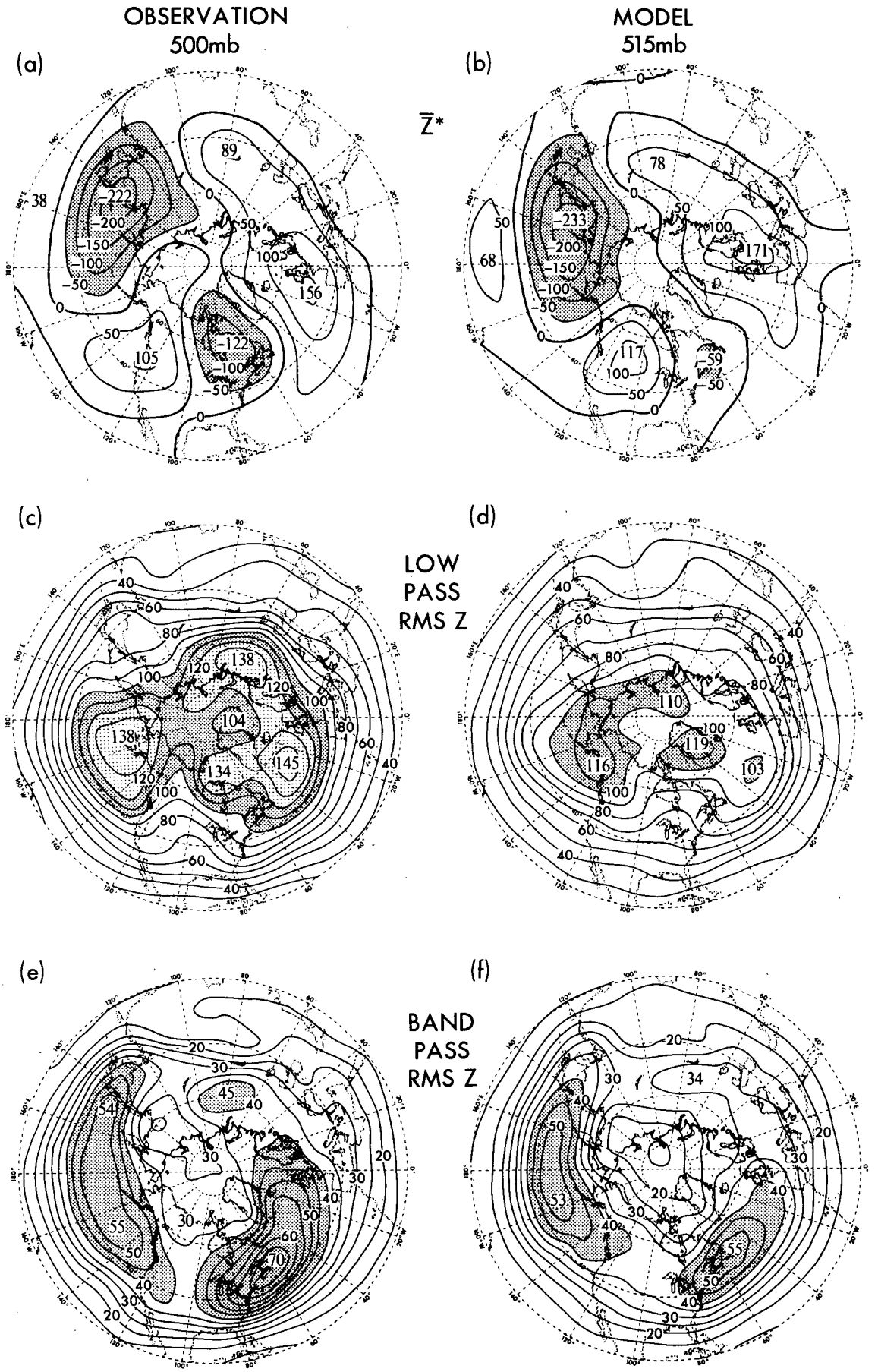
OBSERVATION
500mb
MODEL
515mb
(a)
(b)
$\overline{Z}^*$
(c)
(d)
LOW
PASS
RMS Z
(e)
(f)
BAND
PASS
RMS Z

features are reproduced in the model atmosphere. The amplitude of the simulated trough over eastern North America is considerably weaker than observed, and the model features tend to be shifted slightly east of their observed locations. The prevalent southwest to northeast tilts of the troughs and ridges in the subtropics is evident in both model and observations.

The observed pattern for lowpass root mean squares (Fig. 1c) is characterized by the three maxima over North Pacific, North Atlantic and the northwestern sector of Siberia. The corresponding model pattern (Fig. 1d) also exhibits maximum variability over the northern oceans. However, there is little evidence of the Siberian center in the model result. The level of lowpass variability in the model atmosphere is generally weaker than observed.

The correspondence between model and observations in the bandpass regime may be assessed by examining Figs. 1e and 1f. The locations of the zonally elongated bands of enhanced variability over the midlatitude Atlantic and Pacific in the observed pattern are well simulated, although the model amplitudes are slightly lower. These regions of active synoptic disturbances are located downstream of the stationary troughs over eastern Asia and eastern North America (Figs. 1a and 1b), and correspond to the principal cyclone tracks in the Northern Hemisphere wintertime circulation. The Atlantic storm tracks in both observed and model atmospheres exhibit a notable tendency to extend across Europe into central Asia. Malone et al. (1984, Fig. 15) have also reported similar success of the NCAR GCM in simulating the principal features of bandpass variability.

Comparison between the lowpass and bandpass results indicates that a large fraction of the total observed or simulated variability resides in the spectral band with periods of 10 days and longer. The model appears to be more capable of simulating the bandpass features, whereas the sites of active low-frequency phenomena are not as well reproduced. A similar impression was reported by Blackmon and Lau (1980) based on diagnoses of a grid point GCM at GFDL.

4. Teleconnectivity patterns

Whereas the variance statistics presented in the previous section are useful indicators of those geographical sites where disturbances of a certain time scale attain maximum amplitudes, further data diagnoses are needed to reveal the actual structure and mode of propagation of the fluctuations occurring in such active regions. In this section we shall first identify and compare the centers of action associated with principal modes of variability in the observed and simulated atmospheres. These centers will then serve as reference locations for constructing coherence/phase patterns to be shown in section 5.

The "center of action" mentioned in the preceding paragraph refers to a location where atmospheric perturbations exhibit strong temporal correlations or anticorrelations with the corresponding perturbations at other remote sites. Hence a typical wavelike modal structure is usually composed of two or more such centers scattered over an extensive region. In this study we shall use the objective technique introduced by Wallace and Gutzler (1981, hereafter referred to as WG) to conduct a systematic search for those centers of action. This analysis procedure is reiterated as follows: we shall consider an $N \times N$ correlation matrix $\mathbf{R}$, in which the element R_{ij} represents the temporal correlation coefficient between the time series at the ith grid point and the corresponding time series at the jth grid point. Here N is the total number of grid points in the data domain under investigation. Hence, $\mathbf{R}$ is a symmetric matrix consisting of correlation coefficients between grid points paired by all possible combinations. The ith row of $\mathbf{R}$, denoted as $\mathbf{r}_i$, is an N-dimensional vector composed of correlation coefficients between the ith grid point and all other grid points in the domain. The pattern obtained by mapping the N elements of $\mathbf{r}_i$ on the data grid is often referred to as a "teleconnection chart" with the ith location being the reference point. A careful scan of such a teleconnection pattern should reveal how strongly fluctuations at the ith grid point are correlated with fluctuations elsewhere in the data domain. In particular, a convenient measure of the degree of this "teleconnectivity" associated with the ith grid point is given by the largest negative value (i.e., the minimum) among all the elements in $\mathbf{r}_i$. If we assign the absolute value of this minimum to the ith grid point, and repeat the same procedure for every row of $\mathbf{R}$, we obtain an N-dimensional vector $\mathbf{T}$, with each element T_i being defined as

$$T_i = |(R_{ij}) \text{ minimum for all } j|.$$

The map of $\mathbf{T}$ on the data grid has been referred to as the "teleconnectivity pattern" by WG. Sites of maxima in this map correspond to locations which exhibit strong negative correlations with certain parts of the domain, i.e., these sites are the "centers of action" desired for identifying characteristic modal patterns. In constructing the matrix $\mathbf{R}$, the covariance and variance quantities were obtained for individual 120-day winters. Averages of these seasonal statistics were taken

FIG. 1. Wintertime distributions of the departure from zonal mean of the time averaged geopotential height, for (a) observed data at 500 mb and (b) GCM data at 515 mb, contour interval 50 m; the root mean squares of lowpass filtered geopotential height, for (c) observed data at 500 mb and (d) GCM data at 515 mb, contour interval 10 m; and the root mean squares of bandpass filtered geopotential height, for (e) observed data at 500 mb and (f) GCM data at 515 mb, contour interval 5 m. In all figures shown in this paper, the outermost latitude circle corresponds to 20°N.

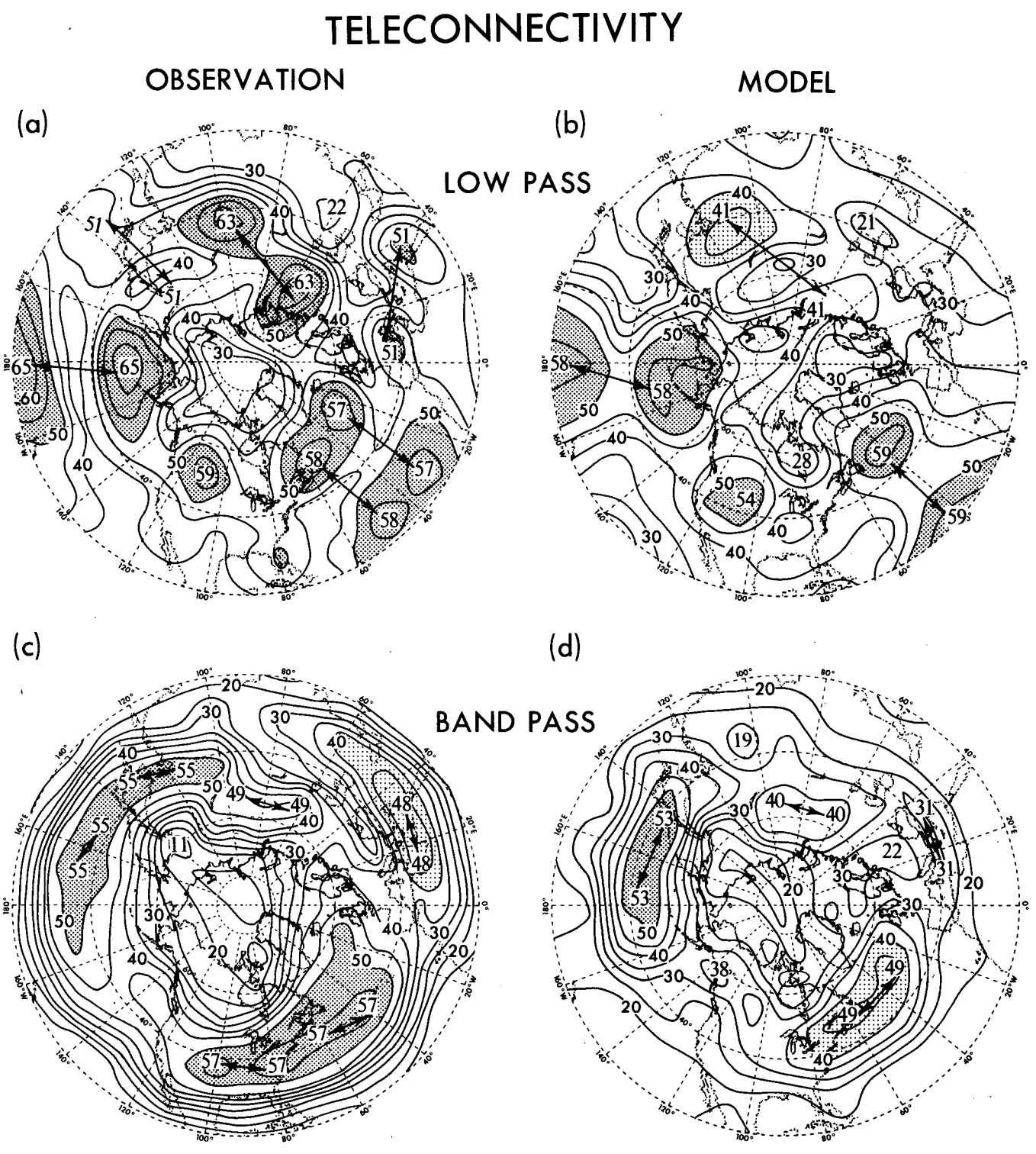

FIG. 2. Wintertime teleconnectivity patterns (see text for explanation) based on lowpass filtered geopotential height, for (a) observed data at 500 mb and (b) GCM data at 515 mb; and on bandpass filtered geopotential height, for (c) observed data at 500 mb and (d) GCM data at 515 mb. Contour interval 0.05. Interrelated centers of action are connected by line segments with arrow heads at both ends.

over 18 winters for the NMC data, and 12 winters for the model data. The resulting ensemble means were then used to evaluate the elements of **R**.

In Fig. 2 are shown the observed teleconnectivity charts for (a) lowpass and (c) bandpass filtered 500 mb geopotential height; the corresponding charts for model

data at 515 mb are displayed in panels (b) and (d). For practical reasons, these results are based on coarser grid meshes with resolutions of 5° (latitude) × 10° (longitude) and 9° (latitude) × 15° (longitude) for the observed and model data, respectively. Bold line segments with arrow heads at both ends are used to highlight pairs of grid points which exhibit particularly strong negative correlations with each other. The observed patterns bear a strong resemblance to the charts presented by Blackmon et al. (1984a, Figs. 12c and 16) on the basis of a slightly different set of winter seasons.

Evident in the observational lowpass results (Fig. 2a) are the following groups of centers of action:

- The pair of Pacific centers along the date line, together with the relatively weaker centers over western Canada and southeastern United States, constitute the well-known "Pacific/North American" (PNA) Pattern noted by WG.
- The two pairs of Atlantic centers, with one pole in each pair being located at about 50°N and the other pole at 25°N, are signatures of the "Eastern Atlantic" (EA) and "Western Atlantic" (WA) Patterns, also noted by WG.
- The two centers located at 60°N, 60°E and 45°N, 100°E have been designated as the "Northern Asian" (NA) Pattern by Esbensen (1984), who further pointed out that this is a feature dominated by intermonthly (as contrasted to interannual) time scales.
- The pair of centers located near the eastern Asian seaboard have been referred to as the Western Pacific (WP) pattern.
- The pair of centers over southern Europe and the Middle East were previously documented by Blackmon et al. (1984a), who suggested the label "Trans-European Pattern" for this phenomenon.

Comparison between the observed lowpass root mean squares (Fig. 1c) and teleconnectivity (Fig. 2a) patterns reveals that the sites of maximum low-frequency variability are coincident with those centers of action in the PNA, EA, WA and NA Patterns lying in the middle and high latitudes.

The simulated lowpass teleconnectivity chart (Fig. 2b) is also characterized by several sets of centers of action. Those teleconnection patterns which bear a notable correspondence with the observations include

- The PNA Pattern, with centers located over the subtropical central Pacific, the Aleutians, and the western United States. The fourth observed center over the southeastern United States is not evident in the simulation.
- The dipole-like configuration straddling 35°N over the Atlantic. In contrast to the observational results, the model data do not indicate a distinct split of this seesaw phenomenon into two pairs of centers over the eastern and western portions of the Atlantic Basin (see Fig. 2a). We shall henceforth refer to this overall structure as the 'Atlantic' (AL) Pattern.
- The Northern Asian (NA) Pattern, with centers of action over northeastern China and just south of the Kara Sea region (65°N, 60°E). The correlation between these two centers is considerably weaker in the model than in the observations. Inspection of individual one-point teleconnection maps based on model data (not shown) indicates that the center over northeastern China is also correlated with the Laptev Sea region near 75°N, 120°E. However, for the sake of comparison with observations, we shall focus our attention on characteristic patterns associated with the somewhat weaker center located near 60°N, 60°E.

For all of the above patterns, there exist minor displacements of the simulated centers of action relative to their observed positions. It is also worth noting that there is no evidence in the model atmosphere of the Western Pacific Pattern noted in WG and the Trans-European Pattern noted in Blackmon et al. (1984a).

The patterns of the teleconnectivity charts based on bandpass data (Figs. 2c and 2d) are radically different from their lowpass counterparts (Figs. 2a and 2b). The observed bandpass result (Fig. 2c) is characterized by three east–west oriented belts of high teleconnectivity. Embedded in each belt are multiple pairs of centers with approximately the same level of correlation. Two of these belts bear a strong resemblance to the elongated maxima in the bandpass rms statistics (Fig. 1e) and are evidently associated with the North America–Atlantic and East Asia–Pacific storm tracks. The third belt extends across the eastern Mediterranean region and is indicative of organized bandpass activity accompanying the enhanced zonal flow in that region (see Blackmon et al., 1977, Fig. 6a). The pattern in Fig. 2c also reveals a zone of rather pronounced bandpass teleconnectivity over Siberia at 55°N between 60° and 110°E.

Most of the observed features described in the preceding paragraph are discernible in the model pattern (Fig. 2d). The simulated extrema over the two oceans tend to be shifted poleward of the observed locations by 5–10° of latitude. The band of activity over the Mediterranean is less evident in the model simulation than in the actual atmosphere.

5. Horizontal phase/coherence patterns in the middle troposphere

In this section we shall examine the horizontal structure and propagation of the fluctuations associated with the centers of action identified in section 4, as well as the frequency dependence of these spatial and temporal relationships. For this purpose we have computed the cross-spectra between the 500 (515 for model) mb height time series at a selected reference point and the corresponding time series at all other points in the Northern Hemisphere. The cospectra, quadrature spectra and power spectra were obtained using the lag-correlation method, with 40 lags for the twice-daily observations, and 20 lags for the once-daily model data.

All spectral quantities were first computed individually for each 120-day winter. These seasonal values were then averaged over 18 winters for the observational data, and 12 winters for the model data. The ensemble means thus obtained were used to estimate the coherence and phase statistics. For each spectral band of interest, the coherences and temporal phase differences between the fluctuations at the chosen reference point and the fluctuations elsewhere are then mapped. The resulting phase/coherence charts are analogous to the one-point teleconnection charts commonly used in various diagnostic studies, the essential distinction being that coherence and phase difference are now plotted instead of linear correlation coefficients.

For the sake of brevity, we shall present such results for only three reference points, each being associated with a distinct and well-defined teleconnection pattern discernible in both the observed and simulated atmospheres. These reference locations have been chosen mainly on the basis of the centers of action appearing in the lowpass teleconnectivity maps displayed in Figs. 2a and 2b. The final selection of the reference points has also been guided by experimentations with phase/coherence maps (such as those shown in Figs. 3–5) based on various reference locations lying in the vicinity of a center of action, so as to determine that particular location which yields the strongest signal. Due to differences in the grid mesh structure for the observational and model datasets, as well as slight discrepancies in the locations of centers of action in the observed and simulated teleconnectivity maps, the reference points chosen for the observations do not exactly coincide with those used for the model. However, such minor displacements do not exceed 12.5° of longitude and 7.75° of latitude in all three cases. The locations of the reference points thus chosen for the actual and simulated atmospheres are listed in Table 1. The lowpass teleconnection patterns which are associated with each of these reference centers are also indicated in Table 1.

The phase/coherence plots for the reference points associated with the PNA, AL and NA teleconnection patterns (see Table 1) are displayed in Figs. 3, 4 and 5, respectively. All results shown here are based on unfiltered geopotential height data at 500 and 515 mb in the observed and simulated atmospheres, respectively. In each figure are shown the observed phase and coherence relationships for the frequency bands centered at periods of (a) 40, (c) 20, (e) 10 and (g) 4 days. The corresponding model patterns are presented in panels (b), (d), (f) and (h). Considering the number of lags used in evaluating these cross-spectral estimates, the width of the individual frequency bands is 0.025 d^{-1}. Hence the 40-day band actually encompasses all periods from 27 to 80 days. Similarly, the period ranges for the bands centered at 20, 10 and 4 days are 16–27, 8.9–11.4 and 3.8–4.2 days, respectively. For the sake of brevity, we shall occasionally refer to these frequency intervals as the 40-, 20-, 10- and 4-day bands. The location of the reference point used in a given panel is indicated by a solid dot in that panel.

For each frequency band considered here, the phase difference between the fluctuations at a certain grid point in the data domain and the fluctuations at the fixed reference location is depicted by the orientation of an arrow plotted at that specific grid point. The convention adopted for orienting the arrows is as follows: an arrow pointing directly at the North Pole indicates zero phase difference between the reference location and the site where that arrow is plotted. The arrows rotate one degree from this due-north orientation for each degree of phase difference between the reference location and the grid point being considered. Clockwise rotations of these arrows indicate a tendency for fluctuations at the arrow site to lag the fluctuations at the reference location, whereas counterclockwise rotations indicate phase leads relative to the reference location. Hence, a westward (eastward) pointing arrow represents a phase lead (lag) of 90° (or a quarter-cycle) relative to the reference point, a southward pointing arrow signifies an exact 180° out-of-phase relationship, and so forth.

Arrows are plotted only over those sites where the squared coherences with the reference location are larger than the threshold value corresponding to the 80% significance level. Grid points with squared coherences exceeding the 95% significance level are highlighted by stippling. In the present study, the length of the data records is $N_0 = 18 \times 240 = 4320$ for the NMC data, and $N_0 = 12 \times 120 = 1440$ for the GCM data. The number of lags used is $m = 40$ for the NMC data, and $m = 20$ for the GCM data. According to Julian (1975), the appropriate number of degrees of freedom, as given approximately by N_0/m, is 108 for the NMC data and 72 for the GCM data. The corresponding squared coherences at the 80 (95)% significance levels are hence 0.122 (0.167) for the NMC data and 0.150 (0.203) for the GCM results (see Panofsky and Brier, 1958).

For each reference point and frequency band examined here, it is seen that all grid points surpassing the squared coherence values cited above lie within 180° of longitude from each other. We therefore present only that half of the data domain which contains all the grid points with statistically significant phase relationships with the reference point. The other half of the domain (not shown) does not contain any grid point with fluctuations which are coherent with the reference location.

For a more quantitative documentation of the lead–lag relationships shown here, those phase differences and squared coherences passing the 95% or 80% significance test are averaged over grid points lying within individual coherent regions, and the resulting values for these selected regions are listed in Tables 2, 3 and 4 for the PNA, AL and NA Patterns, respectively. The regions chosen for computing these areal averages are identified by letters in the alphabet, and their locations

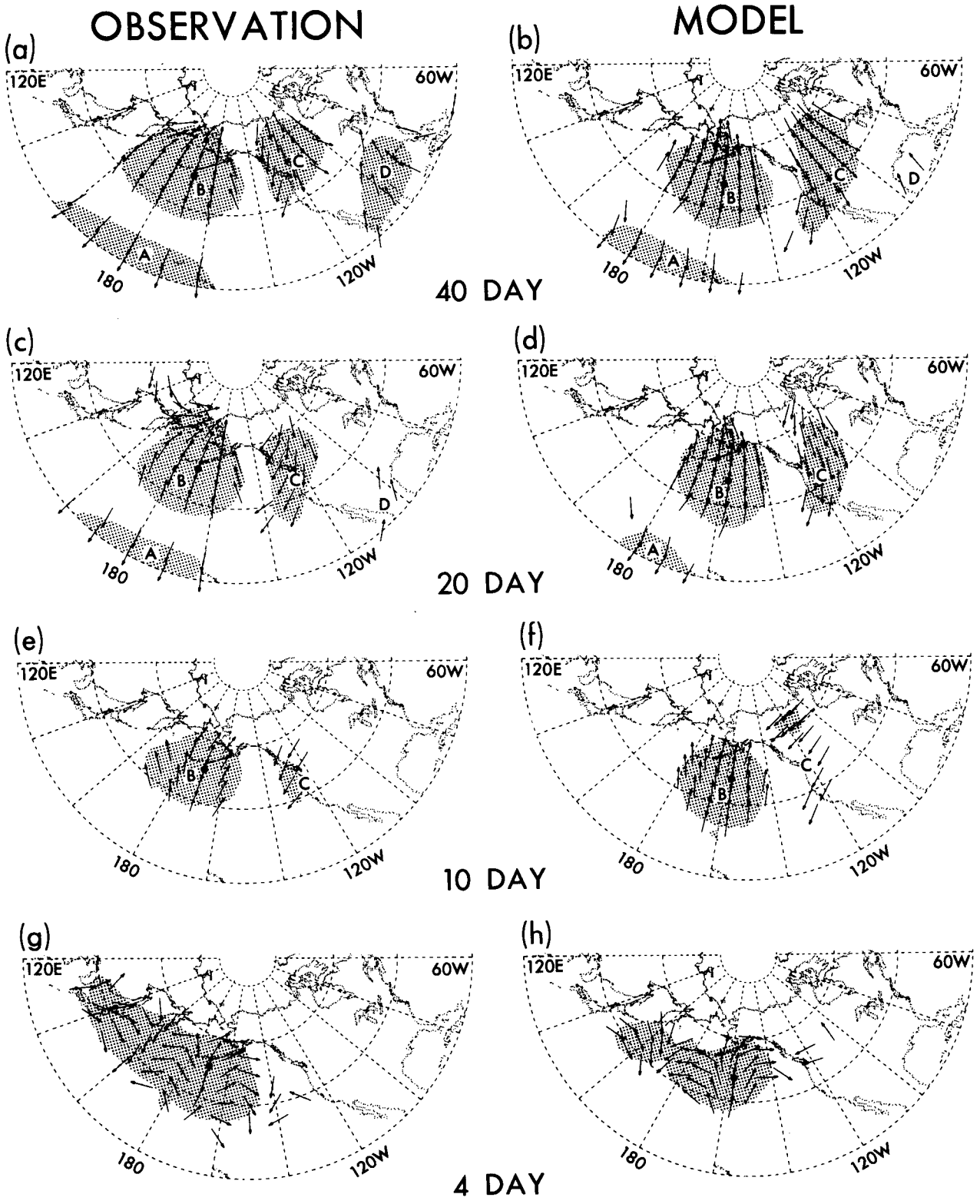

FIG. 3. Phase differences between the wintertime geopotential height fluctuations at the reference point (50°N, 170°W for observations, 47.25°N, 157.5°W for model data, indicated in the appropriate panels by a large dot) and the corresponding fluctuations at all other grid points, as depicted by the orientation of the individual arrows. The results based on observed 500 mb data are shown for the frequency bands with periods centered at (a) 40, (c) 20, (e) 10 and (g) 4 days. The period ranges for these four bands are 27–80, 16–27, 8.9–11.4 and 3.8–4.2 days, respectively. The corresponding patterns based on model data at 515 mb are displayed in panels (b), (d), (f) and (h). The arrows are directed poleward at those grid points where the fluctuations are in phase with the reference point. They rotate clockwise (counterclockwise) by one degree for each degree of phase lag (lead) of the fluctuations at the grid points in question relative to the reference point. Arrows are plotted only at those grid points which are coherent with the reference point at an 80% or higher significance level. Regions with squared coherences exceeding the 95% significance level are indicated by stippling. See text for additional details. Single-letter labels are used to identify various regions with coherent perturbations.

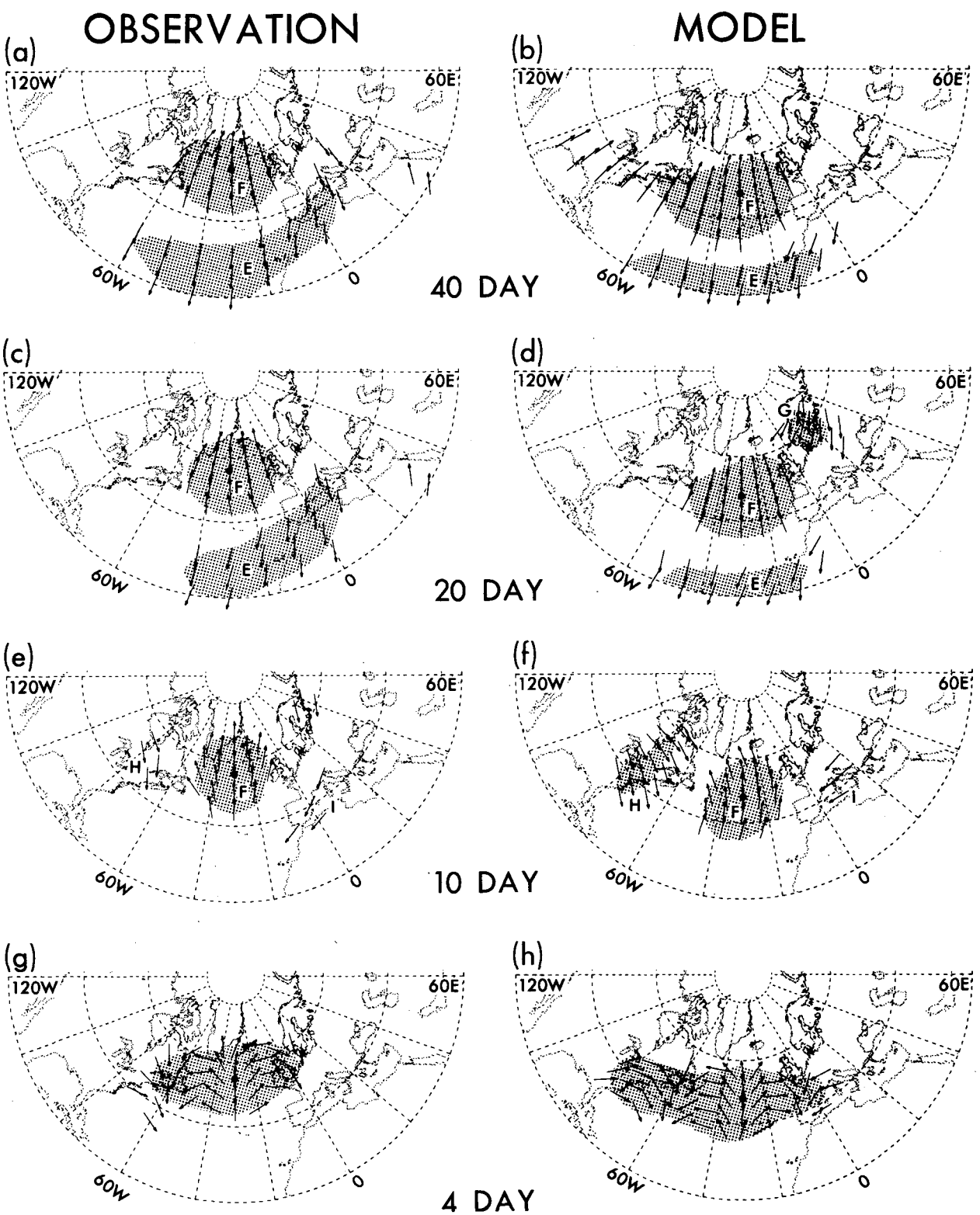

FIG. 4. As in Fig. 3 except for phase/coherence patterns relative to the reference point at 55°N, 30°W for observations, and at 47.25°N, 30°W for model data.

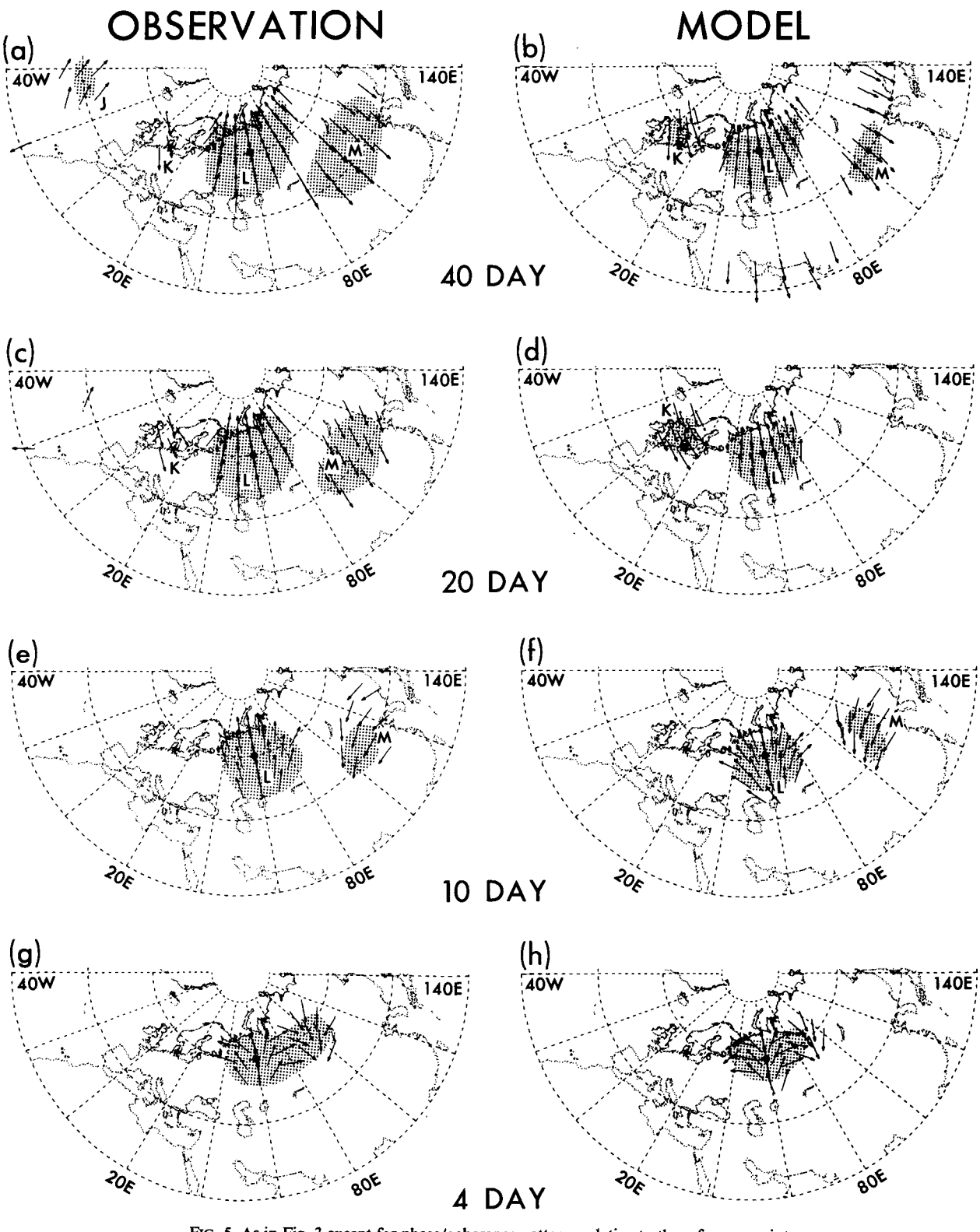

FIG. 5. As in Fig. 3 except for phase/coherence patterns relative to the reference point at 60°N, 60°E for observations, and at 60.75°N, 60°E for model data.

are depicted in the appropriate panels of Figs. 3–5. In these tabulations, the averaged phase for the region containing the reference point (i.e., Region B in Fig. 3, Region F in Fig. 4 and Region L in Fig. 5, hereafter referred to as the reference region) is arbitrarily set to zero, and the phase values for other regions in the same pattern are measured relative to the zero-phase at the reference region. The phase data have been converted to units of days, taking into account that 360° is equivalent to one full period corresponding to the frequency band under investigation. Such conversions have been made using the periods at which the individual frequency bands are centered (i.e., 40, 20, 10 and 4 days). For a given frequency band centered at a period of P days, all the phase values ϕ in Table 2–4 are given within the range $0 \leqslant \phi \leqslant P$.

The manner in which lead–lag relationships may be discerned from Tables 2–4 is best illustrated by several examples. Consider a certain region of interest X and the frequency band centered at $P = 40$ days: a phase value of $\phi = 1$ day would indicate that a signal with that frequency tends to arrive at X one day *after* it arrives at the reference region X_R; whereas $\phi = 39$ days would indicate that a signal tends to arrive at X one day *before* it arrives at X_R. These interpretations may be phrased in more general terms as follows:

- For $\phi \sim 0$, signals of a given polarity would arrive at the region of interest ϕ days *after* signals of the same polarity are detected in X_R.
- For $\phi \sim P$, signals of a given polarity would arrive at the region of interest $P - \phi$ days *before* signals of the same polarity are detected in X_R.

TABLE 2. Area-averaged values of phase difference and squared coherence in different frequency bands and for different coherent regions associated with the Pacific/North American Pattern (PNA, see Fig. 3). Averages are mostly taken over those grid points lying within a given region with coherences exceeding the 95% significance level. For those regions where none of the grid points surpasses the 95% criterion (e.g., Region D in the model pattern for the 40-day band), the averages are taken over all grid points with coherences exceeding the 80% level, and are presented here in parentheses. For easier interpretation, the phase at the reference region B has been set to zero and the phases at all other regions are expressed relative to this reference. The period ranges for the 40-, 20- and 10-day bands are 27–80, 16–27 and 8.9–11.4 days, respectively.

Period (days)	Region	Phase (days)		Squared coherence	
		Observed	Model	Observed	Model
40	A	20.4	19.7	0.30	0.32
40	B	0.0	0.0	0.48	0.52
40	C	21.4	20.6	0.27	0.30
40	D	2.9	(3.2)	0.20	(0.16)
20	A	9.8	10.3	0.27	0.25
20	B	0.0	0.0	0.43	0.50
20	C	12.0	11.7	0.24	0.26
20	D	(2.3)	—	(0.14)	—
10	B	0.0	0.0	0.47	0.50
10	C	6.6	7.3	0.20	0.22

TABLE 3. As in Table 2 except for phase differences and squared coherences in various regions associated with the Atlantic Pattern (AL, see Fig. 4). The phase at the reference region F has been set to zero.

Period (days)	Region	Phase (days)		Squared coherence	
		Observed	Model	Observed	Model
40	E	21.0	21.1	0.26	0.33
40	F	0.0	0.0	0.47	0.54
20	E	11.0	11.0	0.24	0.27
20	F	0.0	0.0	0.45	0.53
20	G	—	13.2	—	0.23
10	H	(3.7)	3.1	(0.14)	0.22
10	F	0.0	0.0	0.48	0.50
10	I	(6.8)	(7.5)	(0.13)	(0.18)

In the ensuing presentation, we shall encounter many situations in which the phase differences between the region of interest X and the reference region X_R is close to a half-period. In such instances, it is more revealing to consider the temporal lags or leads between signals of a given polarity at X and signals of the *opposite* polarity at X_R. For example, it is more convenient to visualize $\phi = 24$ days as indicative of pressure troughs arriving at the region of interest $24 - 40/2 = 4$ days after the appearance of pressure *ridges* in X_R, rather than characterizing the same scenario by the arrival of troughs at the region of interest 24 days after (or 16 days before) the appearance of *troughs* in X_R. Such alternative interpretations may be summarized as follows:

- For $\phi \sim P/2$ and $\phi - P/2 > 0$, signals of a given polarity (say, a pressure "trough" in synoptic terminology) would arrive at the region of interest $\phi - P/2$ days *after* signals of the opposite polarity (i.e., a pressure "ridge") are detected in X_R.
- For $\phi \sim P/2$ and $P/2 - \phi > 0$, signals of a given polarity would arrive at the region of interest $P/2 - \phi$

TABLE 4. As in Table 2 except for phase differences and squared coherences in various regions associated with the Northern Asian Pattern (NA, see Fig. 5). The phase at the reference region L has been set to zero.

Period (days)	Region	Phase (days)		Squared coherence	
		Observed	Model	Observed	Model
40	J	33.9	—	0.19	—
40	K	(14.1)	14.2	(0.14)	0.23
40	L	0.0	0.0	0.54	0.53
40	M	21.1	20.5	0.30	0.23
20	K	6.3	6.0	0.17	0.23
20	L	0.0	0.0	0.52	0.56
20	M	11.3	—	0.26	—
10	L	0.0	0.0	0.47	0.48
10	M	6.8	7.1	0.20	0.22

days *before* signals of the opposite polarity are detected in X_R.

Among the alternatives given after the four bullets in the above discussion, we shall as a rule of thumb choose the interpretation which entails the least amount of temporal lead or lag for given values of P and ϕ.

Prior to discussion of the data shown in Tables 2–4, we emphasize here that the area-averaged phase value for a given coherent region is meaningful only if that region is composed of individual grid points with approximately uniform phases. For those coherent regions in which the phases exhibit considerable variations from one grid point to another, the corresponding averaged phase must be interpreted with caution, especially when the differences between areal averages for two coherent regions of interest are comparable or smaller than the level of phase variability within these two individual regions. An appreciation of the degree of spatial homogeneity of the phase arrows within a given coherent zone may be gained by visual inspection of the patterns in Figs. 3–5. Those regions and frequency bands characterized by excessively large variability of the phase arrows will also be pointed out in the following discussion.

a. Pacific/North American (PNA) pattern

The observed phase/coherence pattern for the 27–80 day band (Fig. 3a) is characterized by four distinct regions of mutually coherent fluctuations. These regions are separated from each other by narrow gaps where the coherence is much weaker. The centroids of these coherent regions are coincident with the four centers of action associated with the PNA Pattern described by WG. The zonal scale of the individual regions appears to be comparable or larger than the meridional scale. With a few exceptions, the arrows in each stippled region are pointed in approximately the same direction, indicating that most grid points within a given coherent region exhibit a similar phase relationship with the reference point (indicated in each panel by a solid dot). The orientation of the arrows undergoes abrupt changes from one coherent region to another. By making use of the synoptic interpretations outlined in the preceding paragraph, it is seen that the set of phase relationships displayed in Fig. 3a and Table 2 portrays the following scenario for sinusoidlike fluctuations with a 40-day period: at time t_0, the appearance in Region B of a positive 500 mb height anomaly is accompanied almost immediately (at time $t_0 + 20.4 - 20 = t_0 + 0.4$ days) by the appearance of a negative anomaly in Region A. This north–south seesaw is then followed by the appearance of a negative anomaly in Region C at time $t_0 + 21.4 - 20 = t_0 + 1.4$ days, and a positive anomaly in Region D at $t_0 + 2.9$ days. Similarly, negative anomalies in Region B tend to precede positive anomalies in Regions A and C by 0.4 and 1.4 days, respectively, and negative anomalies in Region D by 2.9 days. This sequence of temporal evolution is consistent with the lagged teleconnection maps for the PNA Pattern, as presented by Blackmon et al. (1984b, Fig. 6) based on lowpass filtered data.

The simulated phase pattern for the 27–80 day band (Fig. 3b) is also characterized by four regions of coherent variability. Evident in the model pattern and in Table 2 is the nearly out-of-phase relationship between regions A and B. The orientation of the arrows over the Gulf of Mexico, where the coherence is only significant at the 80% level, is also suggestive of a temporal lag of 3.2 days relative to Region B. Within Region C itself, the arrows situated in the southwestern quadrant (i.e., over the Californian coast) tend to lag the arrows in the northeastern quadrant (i.e., over central Canada). Such a phase pattern is indicative of the tendency for fluctuations over Canada to spread southwestward as time advances. A similar phase variation is also discernible in Region C of the observed pattern (Fig. 3a).

For the 20-day period (Fig. 3c), the observed variability over the U.S. Gulf Coast and Mexico becomes less coherent with the other three regions. Variations in regions A and B maintain a near half-period phase difference. Perturbations of a given sign in Region C tend to exhibit a lag of 2 days (or one-tenth of a period) relative to perturbations of the opposite sign in Region B. All of the above characteristics are evident in the corresponding model pattern (Fig. 3d).

For fluctuations with a period of 10 days (Figs. 3e and 3f), the only remaining coherent features are Regions B and C, with troughs (ridges) in Region C lagging ridges (troughs) in Region B by close to one-fifth of a period. The weak clockwise rotation of the phase arrows as one travels eastward across Region B is suggestive of some phase propagation from west to east within that region. The subtropical central Pacific is no longer a coherent zone in both the observed and simulated patterns.

The phase/coherence patterns for the 4-day period in both model and observed atmospheres (Figs. 3g and 3h) are drastically different from the charts for longer periods described above. In sharp contrast to the presence in the low frequency patterns of several distinct coherent zones with approximately uniform phases in each zone, the 4-day perturbations exhibit strong coherences along a single elongated belt over the Pacific, with systematic phase variations within that belt. The location of this coherent zone coincides with that of the wintertime cyclone tracks revealed in the bandpass root mean squares and teleconnectivity patterns (Figs. 1e, 1f, 2c and 2d). It is seen that the arrows undergo a continuous clockwise rotation as one traverses from west to east, thus indicating the prevalence of eastward phase propagation along the storm track. The typical zonal wavelength of these migratory disturbances, as estimated by the distance along a given latitude circle between two arrows with the same orientation, is approximately 60° of longitude. The corresponding phase

speed is ~ 15 m s^{-1}. Close inspection of Figs. 3g and 3h further reveals that, for a given meridian, fluctuations over the grid point at about 50°N tend to lead the corresponding fluctuations over grid points located farther north and farther south. This behavior is more evident in the observed pattern than in the simulated pattern. In synoptic terms, such relationships are indicative of crescent-shaped eddies, with prevalent southwest-to-northeast tilts of the trough and ridge axes south of about 50°N, and northwest-to-southeast tilts in regions farther north. However, such phase variations along a given meridian are considerably weaker than phase variations along a given latitude circle. Hence, in contrast to the low frequency fluctuations, the meridional scale of the individual eddies embedded in the cyclone track is larger than the corresponding zonal scale, and the shape of these eddies is characterized by elongation along the north–south axis. The properties of the observed and simulated bandpass eddies described here are in good agreement with the findings reported by Blackmon et al. (1984a, 1984b) using lagged cross-correlation statistics, and by Wallace and Lau (1985) using anisotropy measures.

b. Atlantic (AL) pattern

In Fig. 4 are shown the phase/coherence patterns with the reference point located at 55°N, 30°W (47.25°N, 30°W) for observed (model) data. For the 27–80 day band [panels (a) and (b)], these patterns are characterized by two coherent and zonally elongated regions in the Atlantic Basin, with the phase of fluctuations over the subtropical Atlantic (western portion of Region E) being shifted by approximately a half-period from that of the reference region F. The grid points at the eastern end of Region E (i.e., North Africa) are seen to lag the grid points situated farther west in the same region. In the model simulation (Fig. 4b), the reference region F extends southwestward to the eastern half of the United States, whereas the corresponding feature in the observed pattern (Fig. 4a) is confined to the North Atlantic.

For a period of 20 days (Figs. 4c and 4d), the north–south oriented dipole over the Atlantic is still discernible. In Region E, deviations of the phase arrows from a due-south orientation are more evident for the 20-day perturbations than for the 40-day perturbations (see also Table 3). The phase relationship between regions E and F described here are consistent with the asymmetry of the teleconnection patterns with positive and negative time lags, as presented for the Eastern Atlantic Pattern in Blackmon et al. (1984b, Fig. 5). A third coherent zone is depicted in the model pattern over Scandinavia (Region G in Fig. 4d), where the fluctuations tend to lag those in Region E by about 2 days.

In the frequency band centered at the 10-day period (Figs. 4e and 4f), fluctuations in the subtropical zone are no longer coherent with fluctuations at the reference point. Instead, most of the grid points with coherent perturbations are situated within an east–west oriented corridor between 40° and 70°N. Both observed and model results are suggestive of a new coherent region in the eastern Canada/northeastern U.S. sector (Region H in Figs. 4e and 4f), and another region over southern Europe (Region I). The phase relationships between these individual zones are such that appearance of an anomaly in a given zone is followed about two days later by the appearance of an anomaly with the opposite polarity in the zone located immediately to the east. The successive downstream development of alternating troughs and ridges in regions H, F and I is reminiscent of the Rossby wave dispersion simulated in barotropic numerical experiments (Hoskins et al., 1977).

Analogous to the situation in the PNA sector, the phase/coherence patterns for the Atlantic Basin change dramatically for periods shorter than 10 days. Fluctuations with a 4-day period (Figs. 4g and 4h) are again organized about the Atlantic storm track. The prevalent eastward phase propagation, zonal wavelength, phase velocity and horizontal shape of the synoptic scale eddies over the Atlantic are essentially similar to those described earlier for the Pacific storm track (Figs. 3g and 3h).

c. Northern Asian (NA) pattern

The phase-coherence charts corresponding to the reference point located at or near 60°N, 60°E are shown in Fig. 5. For the 27–80 day band, four coherent regions are discernible in the observed pattern (Fig. 5a). The phase relationships depicted in that panel and in Table 4 indicate that the appearance of a ridge in Region J at time t_0 tends to be followed by a trough in Region K at $t_0 + 0.2$ days, a ridge in Region L at $t_0 + 6.1$ days, and finally a trough in Region M at $t_0 + 7.2$ days. Similarly, a trough in Region J is followed by a ridge in Region K, a trough in Region L and a ridge in Region M at progressively increasing time lags from west to east. A similar temporal development is portrayed in the model pattern (Fig. 5b). However, the coherent zone over the Atlantic (Region J) is absent from the latter result, and there appears in the simulation an additional coherent region in the Arabian/northwestern Indian sector, where the 40-day fluctuations are out of phase relative to the reference region L.

Inspection of Figs. 5c and 5d indicates that the temporal development for 20-day fluctuations is qualitatively similar to that for the 40-day period. Particularly evident is the large phase differences between the perturbations in regions K and L (see also Table 4). The zone of coherent variability near Mongolia in the observed pattern (Region M) is absent from the model result (Fig. 5d).

The eastward evolution of alternating troughs and ridges across the Atlantic–Europe–Asian sector, as noted above for the 40- and 20-day fluctuations, is

qualitatively similar to the typical sequence of synoptic events occurring just prior to major cold air outbreaks over east Asia, as documented by Joung and Hitchman (1982). However, the characteristic temporal and spatial scales associated with the latter events appear to be shorter than those depicted in Figs. 5a–d.

The phase pattern corresponding to the 10-day period for both observed and simulated data (Figs. 5e and 5f) is indicative of the tendency for troughs (ridges) in Region M to lag ridges (troughs) in Region L by approximately 2 days. Instead of having approximately the same orientation, the phase arrows within the reference region L exhibit a gradual clockwise rotation from west to east, thus inferring some degree of eastward phase propagation within that zone.

Fluctuations in the vicinity of the reference point with 4-day time scales (Figs. 5g and 5h) display many of the characteristics described earlier for the Pacific and Atlantic cyclone tracks (Figs. 3g, 3h, 4g and 4h), except that the longitudinal span over which the eastward migrating disturbances are significantly coherent is considerably shorter in Siberia (i.e., less than one wavelength) than in the maritime regions. It is noteworthy that the coherent regions in Figs. 5g and 5h coincide with a secondary maximum in bandpass variability (Figs. 1e and 1f), and with a site of enhanced teleconnectivity for bandpass filtered data (Figs. 2c and 2d).

6. Vertical phase structure in the middle and lower troposphere

In order to delineate temporal phase variations in the vertical direction, cross spectra have been computed between the time series of 500 (515 for model) mb height at a given grid point and the time series of sea level pressure at the same point. The lag-correlation method has been used to compute the cross-spectral estimates, and the number of lags used was 40 for the NMC data, and 20 for the GCM data. The coherence and phase statistics were evaluated on the basis of ensemble means of spectral quantities determined for individual winters. Analogous to the plotting convention adopted in the previous section, the phase difference between the upper- and lower-level perturbations is indicated by the orientation of an arrow drawn at the grid point in question. A poleward-pointing arrow indicates zero phase difference. The arrows rotate by one degree for each degree of phase difference between 500 (515) mb height and sea level pressure. Clockwise (counterclockwise) rotations depict tendencies for disturbances at the upper level to lag (lead) those at the lower level. Hence an arrow oriented eastward (westward) portrays disturbances with midtropospheric heights lagging (leading) sea level pressure by a quarter-cycle, an arrow oriented southward indicates prevalence of 180° out-of-phase variations between the upper and lower levels, and so on. Arrows are plotted only over those locations where the 500 (515) mb height and sea level pressure exhibit squared coherences which exceed the 80% significance threshold (0.122 for NMC data and 0.150 for GCM data). Regions where the squared coherence values surpass the 95% significance level (0.167 for NMC data and 0.203 for GCM data) are denoted by stippling.

The phase and coherence patterns based on the observed 500 mb height and sea level pressure data are shown in Fig. 6, for the frequency bands with periods centered at (a) 40, (c) 20, (e) 10 and (g) 4 days. The corresponding patterns for the model data are displayed in panels (b), (d), (f) and (h). We, again, note here that the period ranges for these four bands are 27–80, 16–27, 8.9–11.4 and 3.8–4.2 days (see section 5).

The observed and simulated fluctuations in the 27–80 day band exhibit strong coherences in the vertical direction over much of the Pacific and Atlantic Basins, as well as over Europe and northern Siberia (Figs. 6a and 6b). The phase arrows in all these regions are oriented almost directly poleward, indicating the prevalence of in-phase perturbations throughout the middle and lower troposphere on these time scales. It is evident from these results that the coherent 40-day fluctuations in regions A and B associated with the PNA Pattern (Figs. 3a and 3b), regions E and F associated with the AL Pattern (Figs. 4a and 4b), as well as regions K and L associated with the NA Pattern (Figs. 5a and 5b) are characterized by an equivalent barotropic vertical structure.

The phase patterns in Figs. 6c and 6d indicate that the 20-day perturbations are also equivalent barotropic over the central and eastern portions of the two ocean basins, whereas considerable phase differences between 500 (515) mb and the sea level are now discernible over the western oceans and the interior of the Asian and North American land masses. The orientation of the phase arrows in the latter regions infers that the variations at 500 (515) mb tend to lag those at sea level.

For both 10- and 4-day periods (Figs. 6e–6h), the strongest phase differences are located over the eastern Asian seaboard and on the leeward side of the Rockies, with the fluctuations at the upper level lagging those at the lower level by up to a quarter-period. These regions lie close to the starting points of the East Asian/Pacific and North American/Atlantic storm tracks (see Figs. 2e and 2f). For eastward propagating waves, these phase differences are accompanied by westward tilt of the ridge and trough axes with increasing height. The amount of phase tilt is seen to decrease systematically as these waves travel from west to east along the individual storm tracks, so that minimum phase differences are found over those areas where the storm tracks typically terminate (i.e., near the west coast of North America and western Europe). The gradual transition from a strongly baroclinic vertical structure in the western portion of the cyclone tracks to a more baro-

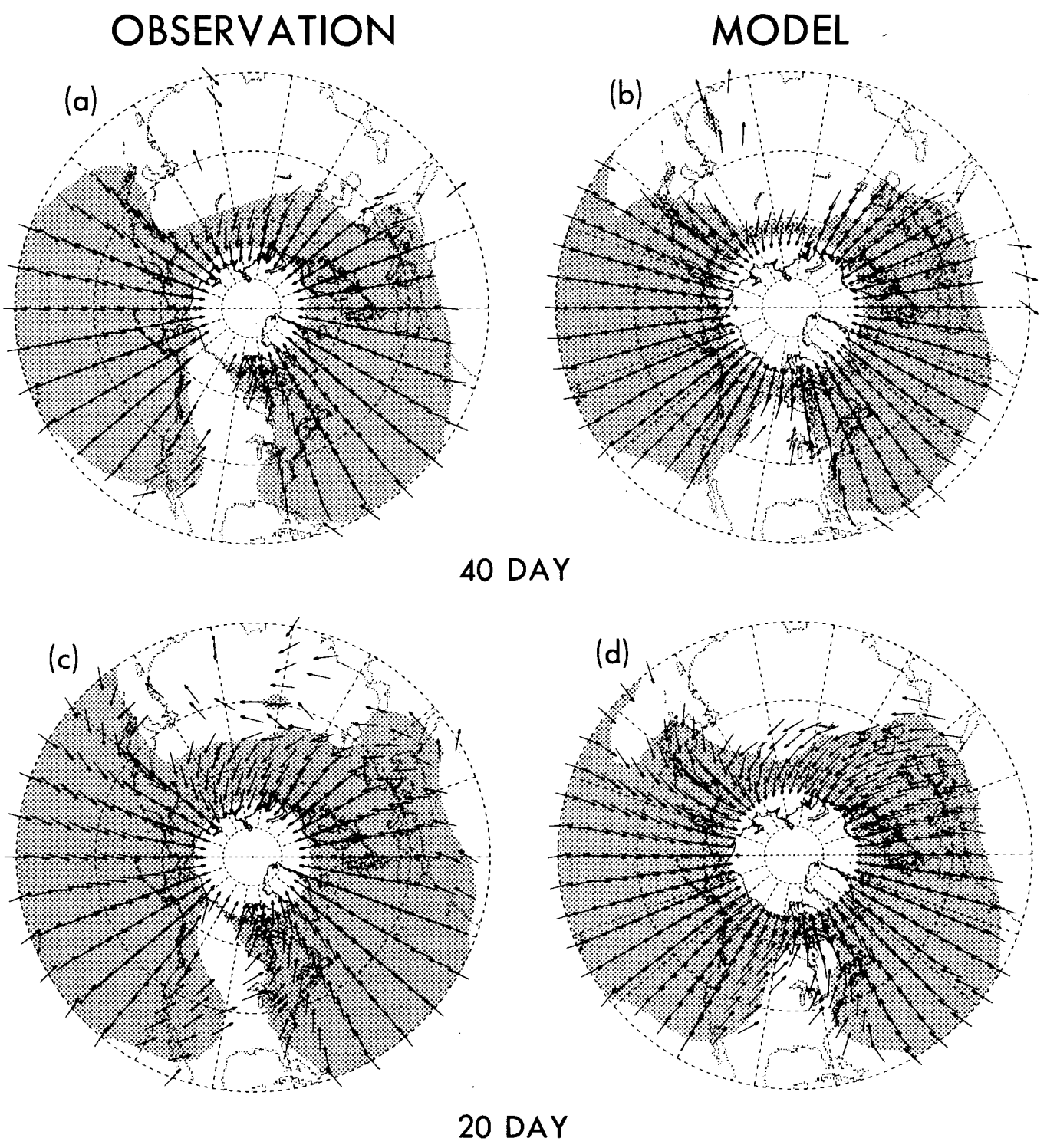

FIG. 6. Phase differences between local fluctuations in 500 (515 for GCM) mb height and in sea level pressure, as depicted by the orientation of the individual arrows. Poleward-pointing arrows indicate an in-phase relationship between fluctuations at 500 (515) mb and at the sea level. The arrows rotate clockwise (counterclockwise) by one degree for each degree of phase lag (lead) of the fluctuations at 500 (515) mb relative to the fluctuations at the sea level for the same grid point. Arrows are plotted only at those grid points where the vertical coherence exceeds the 80% significance level. Regions with squared coherences surpassing the 95% significance level are indicated by stippling. The phase/coherence diagrams based on observed data are shown for the frequency bands with periods centered at (a) 40, (c) 20, (e) 10 and (g) 4 days. The period ranges for these four bands are 27–80, 16–27, 8.9–11.4 and 3.8–4.2 days, respectively. The corresponding patterns based on model data are displayed in panels (b), (d), (f) and (h).

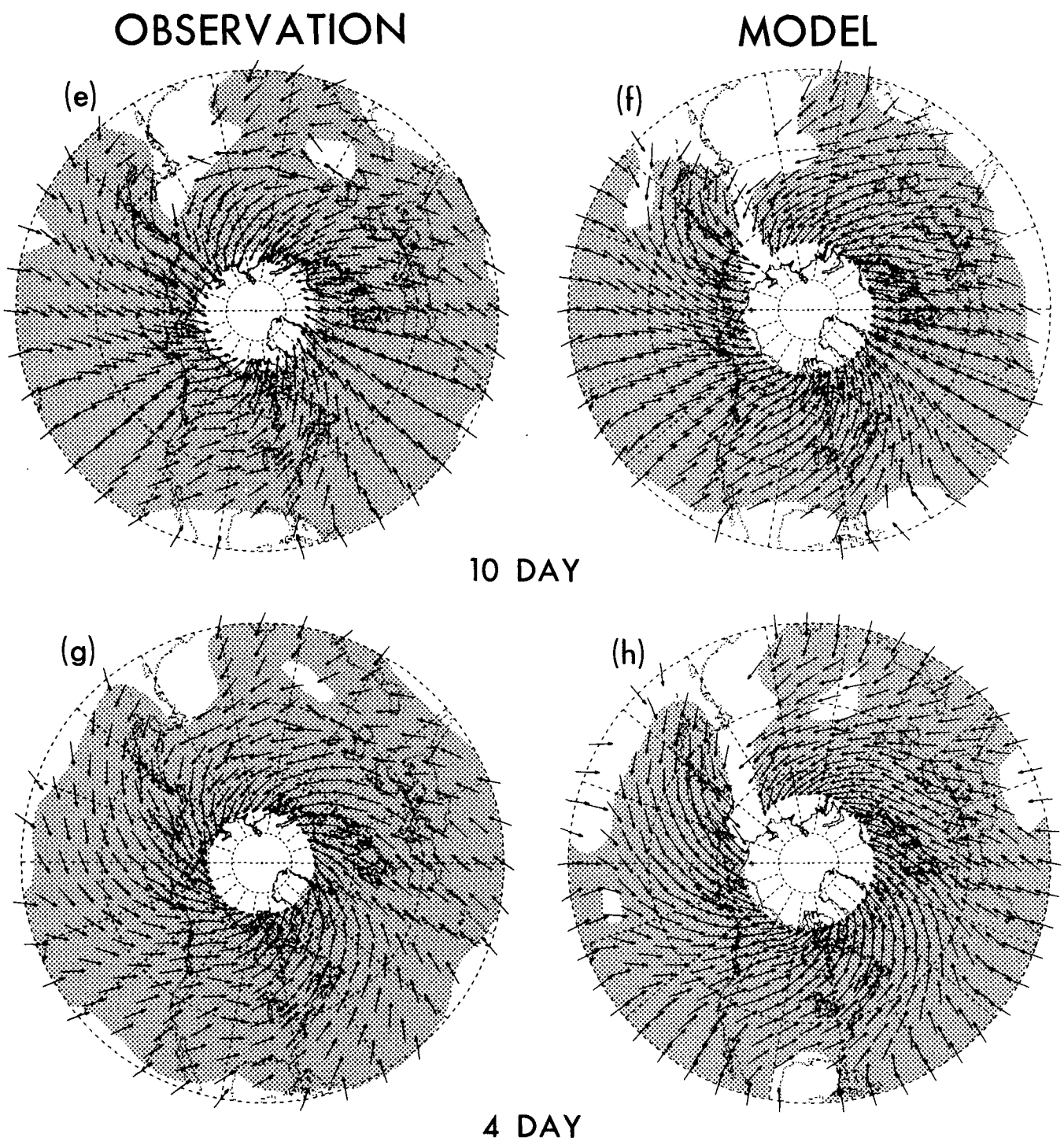

FIG. 6. (*Continued*)

tropic structure at the eastern end is consistent with the numerical experiments performed by Simmons and Hoskins (1978), who noted pronounced structural changes of nonlinear baroclinic waves as they migrate eastward and evolve through a complete life-cycle.

Phase patterns similar to those in Fig. 6 have previously been presented by Lau (1979, Figs. 5 and 6) based on NMC data for geopotential height at 850, 500 and 250 mb, and for periods centered at 5 and 10 days. Despite differences in the pressure levels used, the find-

ings reported therein are in good agreement with the results shown here. The phase relationships depicted in Lau (1979) further indicate that the decrease in the degree of baroclinicity of the eddy structure from west to east along the oceanic storm tracks is just as evident in the 500–250 mb layer as in the 850–500 mb layer. However, the temporal phase differences (or equivalently, the vertical spatial tilt) within the 850–500 mb layer are larger than those within the 500–250 mb layer. The geographical dependence of vertical phase structure depicted in Fig. 6 of the present paper is also consistent with the charts of linear correlation coefficients between observed 1000 and 500 mb heights subjected to different time filters, as presented in Blackmon et al. (1979, Figs. 2 and 3). Particularly noteworthy in the latter study is the prevalence of strong positive correlations over the central and eastern oceans for time scales longer than 10 days, and the near-zero or weakly negative correlations on the leeward side of the Tibetan Plateau and the Rockies for such time scales.

Comparison between the observed and simulated patterns in Fig. 6 indicates that regional contrasts in the vertical phase structures for various time scales are reproduced in the model atmosphere with a reasonable degree of fidelity. For the 10-day and 4-day perturbations, there is some indication that vertical phase differences just east of the Rockies are larger in the real atmosphere (Figs. 6e and 6g) than in the simulated atmosphere (Figs. 6f and 6h).

7. Phase/coherence patterns for sea level pressure over East Asia

Since much of the extratropical oceans in the Northern Hemisphere are characterized by coherent and in-phase vertical structures on 20- and 40-day time scales (see Figs. 6a–6d), one would expect some aspects of the horizontal phase patterns at 500 (515) mb (Figs. 3–5) to be equally discernible at sea level. Indeed, analogous phase/coherence plots based on observed and simulated sea level pressure data for periods of 20 and 40 days (not shown) also exhibit dipole-like structures over the Pacific and Atlantic Oceans. These maritime features bear a strong resemblance to the north–south seesaws in 500 (515) mb height fluctuations between Region A and Region B associated with the PNA Pattern (Figs. 3a–3d), and between Region E and Region F associated with the AL Pattern (Figs. 4a–4d). These characteristic modes of variability in the sea level pressure field have been referred to as the North Atlantic and North Pacific Oscillations by Walker and Bliss (1932), and the surface circulation features accompanying such oscillations have already been extensively documented by Kutzbach (1970), van Loon and Rogers (1978), Rogers (1981) and Trenberth and Paolino (1981), among many others. We have therefore chosen not to present any additional results pertaining to these well-known phenomena. We further note here that, similar to the midtropospheric patterns in Figs. 3g, 3h, 4g and 4h, phase/coherence diagrams for sea level pressure data in the 4-day period (not shown) also indicate coherent, eastward migrating disturbances along well-defined storm tracks over the midlatitude oceans.

The discussion in the preceding paragraph suggests that, for those regions where the upper and lower level fluctuations exhibit strong coherences, the horizontal phase structure at the sea level can more or less be deduced from the corresponding patterns at 500 mb. It is over those regions with weak vertical coherences where one is most likely to uncover near-surface phenomena that are radically different from those portrayed in Figs. 3–5. Inspection of various panels in Fig. 6 reveals that East Asia is one such region. For all four frequency bands examined here, it is seen that the region lying east and north of the Tibetan Plateau is either characterized by weak vertical coherences, or by large phase differences between the upper and lower levels. The behavior of sea level pressure perturbations in this region is delineated in Fig. 7, which shows the phase/coherence patterns corresponding to the 10-day period and based on sea level pressure data of (a) the observed atmosphere, with the reference point located at 37.5°N, 110°E, and for (b) the simulated atmosphere, with the reference point located at 38.25°N, 105°E. The plotting conventions are identical to those adopted for Figs. 3–5. The westward pointing arrows at locations north and west of the reference point in the observed pattern (Fig. 7a) indicate that the sea level pressure signals arrive earliest at such locations. The phase arrows tend to undergo continuous clockwise rotation as one traverses from north to south along a given meridian, thus implying a preferential equatorward propagation of the sea level pressure perturbations on 10-day time scales. Within the meridional band between 90° and 120°E, the fluctuations at 20° N lag those at 65°N by as much as a half-period (i.e., ~5 days). The corresponding model pattern (Fig. 7b) is characterized by a region of coherent fluctuations flanking the northern and eastern periphery of the Tibetan Plateau. The phase pattern within this coherent zone is also indicative of predominant phase propagation from north to south. There is also some evidence of eastward migration (albeit with a phase speed somewhat different from that associated with the equatorward propagation) along the 40°N latitude. The region of coherent perturbations extends as far north as 65°N in the observed pattern, whereas only those simulated disturbances lying south of about 50°N are coherent with fluctuations at the reference point.

Hsu and Wallace (1985) have previously observed the occurrence of organized 5-day averaged sea level pressure perturbations in the vicinity of sloping terrain, with temporal and spatial characteristics which are distinctly different from those in the middle and upper troposphere. The observed principal paths of migration for the near-surface features in East Asia, as constructed

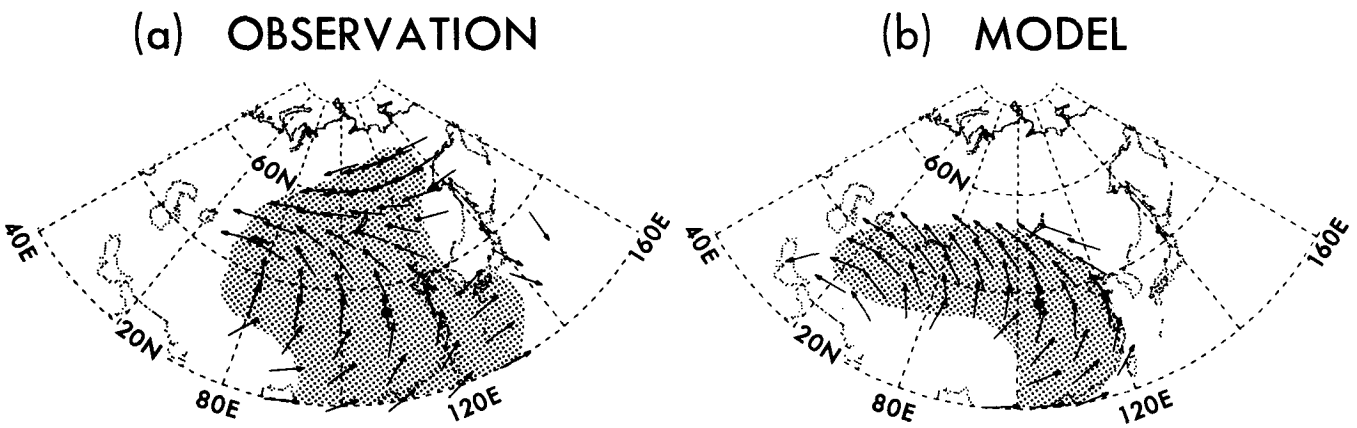

FIG. 7. As in Fig. 3 except for phase/coherence patterns of the sea level pressure field corresponding to the 10-day period. The reference points are located at 37.5°N, 110°E for observations, and at 38.25°N, 105°E for model data (see solid dots in the appropriate panels).

on the basis of lagged correlation charts in Hsu and Wallace's study (see their Fig. 18), also tend to curve around the local terrain in a clockwise fashion as noted in Fig. 7.

8. Discussion

Teleconnectivity charts and phase/coherence diagrams analogous to those shown in Fig. 2 and Figs. 3–5, respectively, have been constructed using summertime data for both the observed and simulated atmospheres. The summer results (not shown) yield teleconnection patterns which are markedly weaker and less organized than the wintertime patterns. Furthermore, the locations of various centers of action in the observed summertime circulation, as inferred from the lowpass teleconnectivity statistics for the 1963–81 period examined here, are in many instances notably different from those documented by Horel (1981, Fig. 5) using rotated principal components derived from monthly averages for the 30 summers from 1950 to 1979. Some of these discrepancies are probably attributable to the analysis methods used and the different time periods covered by the two datasets. In any case, it is worth mentioning here that our present investigation reveals a PNA-like pattern for the 40- and 20-day bands in the observed summertime atmosphere, with three coherent regions located near 40°N, 160°W, the Gulf of Alaska and the Great Lakes Region. The configuration of this pattern is in fair agreement with that associated with Component 4 in Horel's summer result. We also note here that the observed NA Pattern diagnosed for the winter season (see Fig. 5) is also discernible in summer, with comparable spatial and temporal characteristics. On the other hand, this summertime feature is not evident in Horel's study. The model patterns for the summer season are considerably less realistic than those in winter. In particular, there is little resemblance between the observed and simulated teleconnectivity charts, and the model data give no indication of the existence of the PNA and NA Patterns in summer.

An attempt has also been made to diagnose the principal modes of variability in the simulated circulation of the Southern Hemisphere, at both 515 mb and sea level and for both summer and winter seasons. The lack of an extended set of daily observational analyses for the entire Southern Hemisphere has deterred us from comparing the model results with observations in detail. It will suffice to note here that, during the southern winter, the teleconnectivity map based on lowpass filtered model data of 515 mb height is indicative of the occurrence of three north–south oriented dipoles situated over the southern Pacific, Atlantic and Indian Oceans, respectively. Similar features have been detected by Mo and White (1985, Figs. 4 and 6) using monthly averaged Australian analyses. However, contrary to the observational results, the individual dipoles in the model atmosphere exhibit rather weak coherences with each other on 27–80 day time scales. Noticeable discrepancies also exist between model and observations with respect to the precise locations of such dipoles. The comparison between the summertime teleconnectivity chart presented in Mo and White's study (their Fig. 7) and the corresponding model result for 515 mb height (not shown) reveals even more differences. Particularly evident is the absence in the model pattern of the observed centers of action over Australia, South Africa and Brazil.

One of the original motivations for undertaking the present study was to search for some observational evidence for the horizontal phase structure of the barotropically unstable mode associated with the climatological, zonally varying wintertime circulation, as discussed in the numerical study by Simmons et al. (1983). Their investigation indicates that the most rapidly growing mode has a period of about 50 days, and acquires large amplitudes over the Pacific and Atlantic

Oceans, where the horizontal patterns of the fluctuations bear a considerable resemblance to the PNA and EA Patterns, respectively. The temporal evolution of this normal mode is characterized by a quarter-cycle phase lag between the appearance of the PNA signal and that of the EA signal (see their Figs. 11 and 12). Should this planetary scale phenomenon be a principal mode of variability in the observed or GCM atmospheres, one would expect fluctuations over centers of action associated with the PNA Pattern to exhibit significant coherences with those associated with the EA Pattern on 40–50 day time scales, with a quadrature phase difference between the centers over the North Pacific (i.e., Region B in Figs. 3a and 3b) and the North Atlantic (i.e., Region F in Figs. 4a and 4b). As has been noted in section 5, the phase/coherence patterns based on the reference points used in Figs. 3 and 4 do not indicate any occurrence of coherent fluctuations outside the domain shown in these diagrams. Hence, the observational and GCM results presented here offer no direct evidence for any well-defined temporal relationship between the PNA and EA Patterns. It remains to be seen whether other analysis methods which take into account the global nature of the barotropically unstable mode can yield more positive results. However, in view of the diversity of dynamical processes operating in the observed atmosphere as well as in comprehensive GCMs, it might prove to be rather difficult to isolate from such complicated systems the rather idealized anomaly structures identified in mechanistic models.

The spatial and temporal behavior of several well-known teleconnection patterns have been reexamined in this study using cross-spectral analysis techniques. The lead–lag relationships among multiple centers of action associated with a characteristic anomaly pattern have been quantified by tabulating temporal phase differences between different coherent regions for various frequency bands. The spectral approach adopted here has enabled us to determine in one simple step the desired phase relationships for every conceivable frequency range of interest. This shortcut hence bypasses the need for designing various time filters with specific response characteristics, so as to generate datasets which retain certain temporal scales. Furthermore, an adequate description of the temporal evolution of the circulation features in question using such time-filtered datasets would entail the computation of lagged correlation statistics, and the mapping of a multitude of teleconnection patterns, one for each lag. On the other hand, the cross-spectral method allows for all the pertinent information on temporal development within a given frequency band to be presented in a compact fashion by using a single phase/coherence chart, such as those shown in Figs. 3–5. The demonstrable consistency among the findings based on linear correlation statistics in most published studies, and those based on cross-spectral estimates obtained in the present investigation, makes it evident that the spectral approach is a powerful alternative tool for diagnosing atmospheric variability.

In addition to examining the frequency dependence of the spatial and temporal behavior of the observed atmosphere, we have applied the same analysis procedure to a dataset generated by a GCM integration with a duration comparable to that of the observational records. The comparison thus performed should serve as a stringent test of the model performance in reproducing the observed structural and propagation characteristics in different frequency regimes. It is seen that, even to this degree of sophistication, the fluctuations in the model atmosphere compare favorably with their observed counterparts. The considerable agreement between observations and model simulation lends further credence to the current generation of GCMs as useful tools for studying various facets of atmospheric variability.

Acknowledgments. We would like to thank Y. Hayashi, T. Knutson, A. Oort and the official reviewers for reading the manuscript and offering constructive comments. We are also indebted to J. Conner and the GFDL Scientific Illustration Group for preparing the figures, and to J. Kennedy for typing the manuscript.

REFERENCES

Blackmon, M. L., 1976: A climatological spectral study of the 500 mb geopotential height of the Northern Hemisphere. *J. Atmos. Sci.*, **33**, 1607–1623.

——, and N-C. Lau, 1980: Regional characteristics of the Northern Hemisphere wintertime circulation: A comparison of the simulation of a GFDL general circulation model with observations. *J. Atmos. Sci.*, **37**, 497–514.

——, R. A. Madden, J. M. Wallace and D. S. Gutzler, 1979: Geographical variations in the vertical structure of geopotential height fluctuations. *J. Atmos. Sci.*, **36**, 2450–2466.

——, J. M. Wallace, N-C. Lau and S. L. Mullen, 1977: An observational study of the Northern Hemisphere wintertime circulation. *J. Atmos. Sci.*, **34**, 1040–1053.

——, Y-H. Lee and J. M. Wallace, 1984a: Horizontal structure of 500 mb height fluctuations with long, intermediate and short time scales. *J. Atmos. Sci.*, **41**, 961–979.

——, ——, —— and H-H. Hsu, 1984b: Time variation of 500 mb height fluctuations with long, intermediate and short time scales as deduced from lag-correlation statistics. *J. Atmos. Sci.*, **41**, 981–991.

Esbensen, S. K., 1984: A comparison of intermonthly and interannual teleconnection in the 700 mb geopotential height field during the Northern Hemisphere winter. *Mon. Wea. Rev.*, **112**, 2016–2032.

Frederiksen, J. S., 1979: The effects of long planetary waves on the regions of cyclogenesis: Linear theory. *J. Atmos. Sci.*, **36**, 195–204.

——, 1982: A unified three-dimensional instability theory of the onset of blocking and cyclogenesis. *J. Atmos. Sci.*, **39**, 969–982.

——, 1983: A unified three-dimensional instability theory of the onset of blocking and cyclogenesis. II: Teleconnection patterns. *J. Atmos. Sci.*, **40**, 2593–2609.

Gordon, C. T., and W. F. Stern, 1982: A description of the GFDL global spectral model. *Mon. Wea. Rev.*, **110**, 625–644.

Hayashi, Y., and D. G. Golder, 1977: Space–time spectral analysis of midlatitude disturbances appearing in a GFDL general circulation model. *J. Atmos. Sci.*, **34**, 237–262.

Horel, J. D., 1981: A rotated principal component analysis of the interannual variability of the Northern Hemisphere 500 mb height field. *Mon. Wea. Rev.*, **109**, 2080–2092.

Hoskins, B. J., and D. J. Karoly, 1981: The steady linear response of a spherical atmosphere to thermal and orographic forcing. *J. Atmos. Sci.*, **38**, 1179–1196.

——, A. J. Simmons and D. G. Andrews, 1977: Energy dispersion in a barotropic atmosphere. *Quart. J. Roy. Meteor. Soc.*, **103**, 553–567.

Hsu, H-H., and J. M. Wallace, 1985: Vertical structure of wintertime teleconnection patterns. *J. Atmos. Sci.*, **42**, 1693–1710.

Joung, C. H., and M. H. Hitchman, 1982: On the role of successive downstream development in East Asian polar air outbreaks. *Mon. Wea. Rev.*, **110**, 1224–1237.

Julian, P. J., 1975: Comments on the determination of significance levels of the coherence statistic. *J. Atmos. Sci.*, **32**, 836–837.

Klein, W. H., 1951: A hemispheric study of daily pressure variability at sea level and aloft. *J. Meteor.*, **8**, 332–346.

Kutzbach, K. E., 1970: Large-scale features of monthly mean Northern Hemisphere anomaly maps of sea-level pressure. *Mon. Wea. Rev.*, **98**, 708–716.

Lau, N-C., 1978: On the three-dimensional structure of the observed transient eddy statistics of the Northern Hemisphere wintertime circulation. *J. Atmos. Sci.*, **35**, 1900–1923.

——, 1979: The structure and energetics of transient disturbances in the Northern Hemisphere wintertime circulation. *J. Atmos. Sci.*, **36**, 982–995.

——, 1981: A diagnostic study of recurrent meteorological anomalies appearing in a 15-year simulation with a GFDL general circulation model. *Mon. Wea. Rev.*, **109**, 2287–2311.

Malone, R. C., E. J. Pitcher, M. L. Blackmon, K. Puri and W. Bourke, 1984: The simulation of stationary and transient geopotential-height eddies in January and July with a spectral general circulation model. *J. Atmos. Sci.*, **41**, 1394–1419.

Manabe, S., and D. G. Hahn, 1981: Simulation of atmospheric variability. *Mon. Wea. Rev.*, **109**, 2260–2286.

Mo, K. C., and G. H. White, 1985: Teleconnections in the Southern Hemisphere. *Mon. Wea. Rev.*, **113**, 22–37.

Namias, J., 1981: Teleconnections of 700 mb height anomalies for the Northern Hemisphere. *California Cooperative Oceanic Fisheries Investigations Atlas No. 29*, A. Fleminger, Ed., Scripps Institution of Oceanography, La Jolla, CA 92093.

O'Connor, J. F., 1969: Hemispheric teleconnections of mean circulation anomalies at 700 mb. *ESSA Tech. Rep. WB-10*, U.S. Weather Bureau, U.S. Govt. Printing Office, Washington, D.C., 20402. [NTIS N69-34858].

Panofsky, H. A., and G. W. Brier, 1958: *Some Applications of Statistics to Meteorology.* Pennsylvania State University, 224 pp.

Pratt, R. W., 1979: A space–time spectral comparison of the NCAR and GFDL general circulation models to the atmosphere. *J. Atmos. Sci.*, **36**, 1681–1691.

Rogers, J. C., 1981: The North Pacific Oscillation, *J. Climatol.*, **1**, 39–57.

Sawyer, J. S., 1970: Observational characteristics of atmospheric fluctuations with a time scale of a month. *Quart. J. Roy. Meteor. Soc.*, **96**, 610–625.

Simmons, A. J., and B. J. Hoskins, 1978: The life cycles of some nonlinear baroclinic waves. *J. Atmos. Sci.*, **35**, 414–432.

——, J. M. Wallace and G. W. Branstator, 1983: Barotropic wave propagation and instability, and atmospheric teleconnection patterns. *J. Atmos. Sci.*, **40**, 1363–1392.

Trenberth, K. E., 1981: Observed Southern Hemisphere eddy statistics at 500 mb: Frequency and spatial dependence. *J. Atmos. Sci.*, **38**, 2585–2605.

——, and D. A. Paolino, Jr., 1981: Characteristic patterns of variability of sea level pressure in the Northern Hemisphere. *Mon. Wea. Rev.*, **109**, 1169–1189.

van Loon, H., and J. C. Rogers, 1978: The seesaw in winter temperatures between Greenland and Northern Europe. Part I: General description. *Mon. Wea. Rev.*, **106**, 296–310.

Walker, G. T., and E. W. Bliss, 1932: World Weather V. *Mem. Roy. Meteor. Soc.*, **4**, 53–84.

Wallace, J. M., and D. S. Gutzler, 1981: Teleconnections in the geopotential height field during the Northern Hemisphere winter. *Mon. Wea. Rev.*, **109**, 784–812.

——, and N-C. Lau, 1985: On the role of barotropic energy conversion in the general circulation. *Adv. Geophys.*, **28A**, 33–74.

White, G. H., 1982: An observational study of the Northern Hemisphere extratropical summertime general circulation. *J. Atmos. Sci.*, **39**, 24–40.